Research Square

Preprints are preliminary reports that have not undergone peer review.
They should not be considered conclusive, used to inform clinical practice,
or referenced by the media as validated information.

Rates of Antarctic Ice Sheet thinning since Last Glacial Maximum rival future projections

Roger Creel

roger.creel@tamu.edu

Texas A&M University

Ryan Venturelli

Colorado School of Mines https://orcid.org/0000-0001-9548-0382

Anna Ruth Halberstadt

University of Texas at Austin

Samuel Chester

Lamont Doherty Earth Observatory https://orcid.org/0009-0009-6195-9040

Ava Nordgren

Colorado School of Mines

John Schiavo

Colorado School of Mines

Physical Sciences - Article

Keywords:

Posted Date: May 4th, 2026

DOI: https://doi.org/10.21203/rs.3.rs-9510920/v1

License: This work is licensed under a Creative Commons Attribution 4.0 International License.
Read Full License

Additional Declarations: There is **NO** Competing Interest.

Rates of Antarctic Ice Sheet thinning since Last Glacial Maximum rival future projections

Roger Creel[1*], Ryan Venturelli[2], Anna Ruth Halberstadt[3], Sam Chester[4], Ava Nordgren[2], John Schiavo[2]

[1]Department of Geology and Geophysics, Texas A M University, 3115 TAMU , College Station, 77843, Texas, USA.
[2]Geology and Geological Engineering, Colorado School of Mines, Berthoud Hall 411E, Golden, 80401, Colorado, USA.
[3]Department of Earth Planetary Sciences, Jackson School of Earth Sciences, University of Texas at Austin, 2305 Speedway Suite 2.112, Austin, 78712, Texas, USA.
[4]Lamont-Doherty Earth Observatory, Columbia University of New York, 61 Route 9W, Palisades, 10964, New York, USA.

*Corresponding author(s). E-mail(s): roger.creel@tamu.edu;

Abstract

Reconstructions of past Antarctic Ice Sheet thinning are ground-truthed using geologic records from terrestrial cosmogenic nuclide measurements[1]. However, rates of cosmogenic nuclide thinning have historically been oversimplified with linear approximations; and how past rates compare to projected future change remains poorly understood, as does the degree to which local thinning profiles capture regional trends[2]. We reconstruct Antarctic Ice Sheet thinning since Last Glacial Maximum using 766 quality-controlled cosmogenic nuclide measurements at 147 sites across Antarctica, then compare past thinning to modern and projected rates at adjacent ice streams using the ICESat-2 observational record[3] and ISMIP-6 projections[4, 5]. When aggregated, cosmogenic nuclide profiles capture regional trends that align with global climate fluctuations and yield rate distributions whose time dependence offers quantitative insight into driving processes. Under sustained high emissions, maximum postglacial rates are 61%(59–63%, 95% credible interval) likely to exceed modern rates, 53%(46–60%) likely to exceed rates by 2100, but only 16%(11–22%) likely to exceed rates by 2300. Our results indicate that Antarctica may soon thin faster than it has since Last Glacial Maximum—a finding with implications for which Antarctic areas will next become ice free.

Key Points

1. Maximum rates of postglacial Antarctic thinning are similar to maximum 21st century thinning rates but are exceeded by future thinning rates between 2100 and 2300 under sustained high emissions.
2. Terrestrial cosmogenic nuclide exposure age data record regional Antarctic thinning patterns that align with global climate fluctuations.
3. Comparison of the timescale dependence of thinning rates in modeled and observed Antarctic thinning profiles yields quantitative insight into driving processes.

1 Main

Determining the rate and timing of Antarctic Ice Sheet (AIS) change during the pre-satellite era represents a major goal of paleoclimatic research [6]. Despite substantial advances, first-order questions remain underconstrained: How rapidly did grounded ice in Antarctica thin during the last deglaciation? Where and when did this thinning occur? What can these patterns reveal about ice sheet response to external

forcings? What context can past thinning provide for future change? These questions have been partially addressed by numerical modeling [7], observational studies [8–10], and data-model syntheses [11, 12], but have not been considered across timescales or with explicit linkage to modern and future change.

A direct window into past Antarctic thinning comes from terrestrial cosmogenic nuclide (TCN) exposure age observations from emergent nunataks [13]. Both as individual thinning profiles [14–16] and aggregated regionally [17], TCN exposure data have been used to elucidate Antarctic deglaciation. Synoptic analyses of TCN records at pan-Antarctic scale [e.g. 18] was recently made feasible through development of the Informal Cosmogenic-nuclide Exposure-age Database [ICE-D, 19], a transparent middle-layer data management tool that dynamically calibrates TCN observations into chronologic constraints on geologic processes, including glacial thinning.

TCN observations of past ice thickness provide point data that by nature are sparse in space and time. To gain temporal and spatial perspective, it is therefore necessary to interpolate between TCN data to elucidate rates of thinning and compare differences between sites to address spatial dynamics. Historically, temporal thinning rates have been extracted from TCN data with a variety of linear techniques, including linear regression [20], probabilistic linear regression [21, 22], piecewise linear regression [23], and visual analysis [24–28]. While linearity assumptions are acknowledged to oversimplify ice thinning dynamics [e.g. 23], their application remains standard [21, 29].

Spatially, TCN data are commonly taken to represent regional thinning patterns that can be compared continental ice sheet simulations[17]. This comparison faces two challenges. First, the ice thinning patterns that TCN data record are sensitive to local factors like katabatic winds, insolation patterns, and ice stream behavior, such that different faces of a single nunatak may record thinning pulses offset by thousands of years [2]. It has therefore remained unclear how much information TCN data hold about regional ice thickness changes. Second, continent-scale postglacial AIS simulations have spatial resolution that is too coarse (20-40 km / pixel) to resolve heterogeneities of ice physics at nunatak-scale [1, 21, 30, 31]. Ongoing difficulties in validating AIS models of this coarseness with TCN data have underscored the likelihood that the TCN record of AIS thinning, which generally proceeds at local-scale with heterogeneous timing, differs in kind from the general regional coherence in modeled AIS thinning [17, 31]. Focus on comparison of continental ice sheet behavior to linearized TCN thinning profiles has obscured the critical information that these profiles can yield about non-linearities in local Antarctic Ice Sheet thinning rates, spatial coherence (or lack thereof) in these rates, and how past rates compare to contemporary and future analogues.

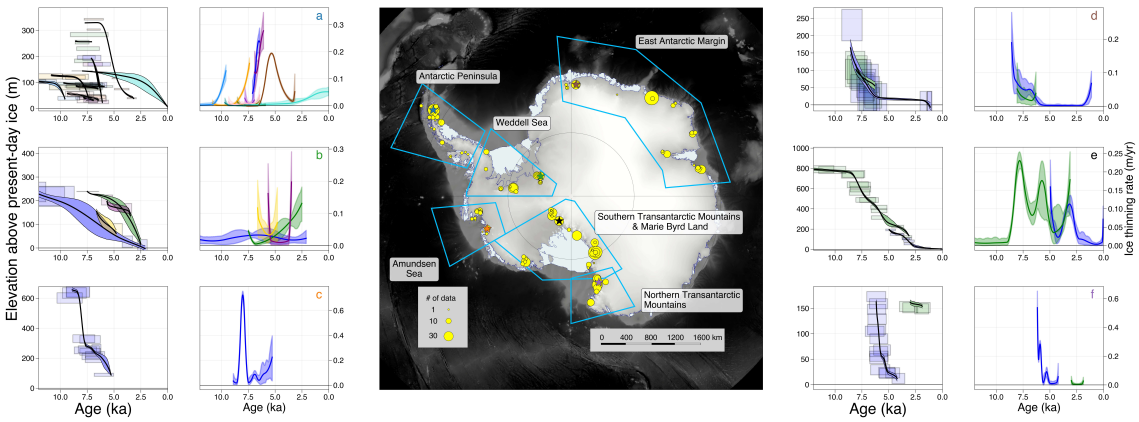


Fig. 1 Cosmogenic nuclide exposure data distribution and example thinning profiles. (center panel) Geographic distribution of cosmogenic exposure age data from the ICE-D database [19]. Dot size denotes number of data per site, with sites representing single cosmogenic nuclide transects. Colored stars mark example clusters from each region (blue polygons), including the Antarctic Peninsula (panel a), Weddell Sea Embayment (b), Amundsen Sea Embayment (c), East Antarctic margin (d), South Transantarctic Mountains and Marie Byrd Land (e), and North Transantarctic Mountains (f). **(panels a - f)** Colored boxes represent cosmogenic exposure data used to fit penalized splines; colored envelopes represent median and 95% credible interval spline fits to single sites. At each example cluster, left panels show ice elevation through time, right panels mark rate of ice thinning. For individual site identifications and data from each site, see Supplementary Information.

2 The Pan-Antarctic ice thinning reconstruction

Here, we harness TCN exposure data to assess non-linear thinning rates across Antarctica over the last 20,000 years and use these rates as context for modern and future Antarctic thinning. The resulting Pan-Antarctic ice-thinning reconstruction (PATR) offers the first proxy-derived view of time-varying

thinning across Antarctic over the last 20 kyr. The PATR enables us to diagnose regional patterns of Antarctic thinning, refine understanding of pan-Antarctic thinning across the Holocene, and compare modern Antarctic change under anthropogenic forcing with the rates of change etched into the recent geologic record.

In assembling TCN exposure data, we leverage the ICE-D Antarctica. To ensure high data quality, we apply screening protocols, including preferencing in situ ^{14}C over $^{10}Be/^{26}Al$ measurements where available; rejecting ^{3}He and ^{36}Cl ages [32]; and discarding samples whose TCN ages indicate inheritance or whose field position indicates post-depositional disturbance (see Methods). The resulting TCN dataset is augmented with complimentary data from radiocarbon-dated proglacial lakes [33] and an absolutely dated ice rise core [34].

The size and spatiotemporal coverage of our proxy thinning compilation yields fresh insight into the LGM-to-present AIS evolution on its own. However, non-linear statistical modeling enables us to leverage these discrete data to discern continuous ice thinning information at local, regional, and pan-Antarctic scales. To extract this information, we divide the vetted compilation into coherent thinning profiles. We construct these profiles following the principle that the noisy local forcing factors that hampered previous application of non-linear models to TCN data [20] can be minimized by granularizing TCN data to individual profiles sampled from single faces of nunataks. To ensure that profiles have sufficient data to inform our reconstruction, we require that profiles be at least 200 years long, consist of at least two datapoints, and have absolute age constraints from ^{10}Be and/or ^{14}C measurements. In total, our vetted compilation consists of 147 sites from the East and West Antarctic Ice Sheets (EAIS, WAIS) as well as the Antarctic Peninsula (AP, Figure 1). We generate smooth thinning histories at each site by constructing a probabilistic statistical framework based on penalized cubic splines that enforces standard glaciological interpretations of the TCN record, including that ice thins monotonically from LGM onwards; that profiles extend from highest to lowest observation; and that thinning profiles pass younger and higher than each TCN observation (see Methods). The hierarchical structure of our Bayesian framework allows us to thoroughly quantify uncertainties on data and parameter layers, which enables an integrated assessment of the robustness of the thinning signals we reconstruct (Supplementary Figure **??**). Thinning profiles are then aggregated regionally, accounting for spatial clustering, and assessed region-by-region both for the fraction of sites reporting AIS thinning through time (Figure 2) as well as the time-averaged fraction of AIS thinning completed (Figure 3a). In interpreting these records, we assume that while isolated changes in thinning rate at single sites can be explained by local processes, synchronous shifts in thinning rate across multiple sites imply regional ice sheet behavior.

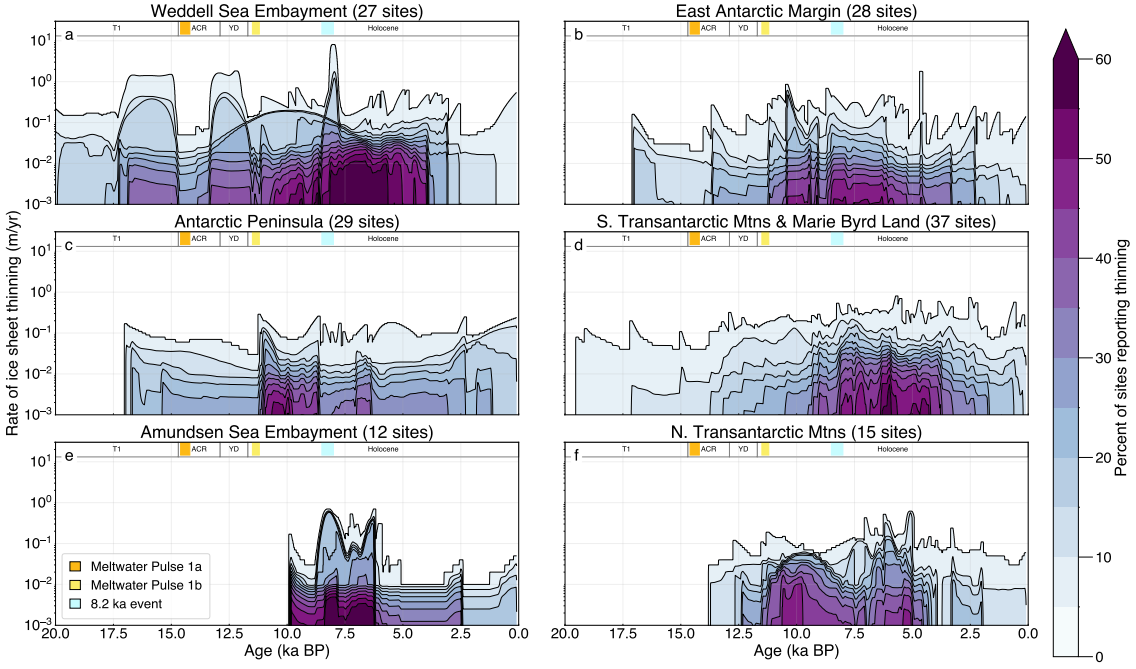


Fig. 2 Rates of regional Antarctic Ice Sheet thinning since Last Glacial Maximum. Colorbar delineates percent of sites thinning in the (a) Weddell Sea Embayment, (b) East Antarctic Margin, (c) Antarctic Peninsula, (d) South Transantarctic Mountains and Marie Byrd Land, (e) Amundsen Sea Embayment, and along (f) North Transantarctic Mountains. Note the logarithmic scale for thinning rates. Time periods in horizontal bar at top of each subplot include Termination 1 (T1), Meltwater Pulse 1a (orange bar), the Antarctic Cold Reversal (ACR), the Younger Dryas (YD), Meltwater Pulse 1b (yellow bar), the 8.2 ka event (blue bar), and the Holocene.

Antarctic Ice Sheet thinning is first recorded in the Weddell Sea Embayment (WSE) and South Transantarctic Mountains / Marie Byrd Land (STaM/MB) at ∼20 ka (Figures 2 and 3), followed by Antarctic Peninsula (AP) and East Antarctic Margin (EA) at ∼17 ka, the North Transantarctic Mountains (NTaM ∼14 ka), and Amundsen Sea Embayment (ASE, ∼10 ka). WSE thinning occurs in ∼2.5 kyr pulses starting at 17.5 ka, 13.5 ka, and 10.5 ka, in which 30+% of sites report thinning. In the mid-Holocene, WSE thinning intensifies, with peak thinning by rate and site percentage reached from 8.5 to 7.5 ka, widespread (50%+ of sites) thinning continuing until 5 ka, and waning thinning until ∼3 ka. EA and AP thinning remains generally constant until the Holocene, after which both sectors broadly follow the WSE, with a pulse of thinning 8.5–7.5 ka and sustained thinning until 2.5-3 ka. STam/MB thinning expands gradually until ∼9 ka, rapidly until ∼7 ka, then gradually tapers to the present. By contrast, along the NTaM, thinning occurs in two phases, the first phase peaking around ∼10 ka and waning by 7 ka, the second peaking from 6 to 5 ka and concluding after ∼4 ka. Finally, ASE thinning is characterized by two peak pulses, the first 8.5–7.5 ka, the second from ∼7-6.5 ka, followed by slower but still widespread thinning until ∼2.5 ka.

3 Climatic events recorded in Antarctic thinning

The Antarctic Ice Sheet, once considered a passive responder to global climatic teleconnections [35], has more recently been recast as a sensitive bellwether for Earth system fluctuations whose responses to oceanic [36–38], atmospheric [39], and solid Earth [40–42] forcings vary temporally, on timescales from hours [43] to glacial cycles [44–46], and spatially even within a single drainage basin [2]. Given the multiple processes driving Antarctic change, it is to be expected that Antarctic thinning should also vary across scales—an expectation that our results confirm. This variability, however, necessitates a thorough evaluation of what TCN thinning profiles represent: local dynamics, regional thinning, or even continental contributions to global mean sea level. Understanding which temporal frequency dominates TCN thinning profiles matters because of the leading role TCN data play in groundtruthing paleo-AIS models [1, 7, 30, 47].

Despite being sensitive to local ice dynamics, TCN profiles in aggregate nevertheless reveal regional AIS thinning patterns (Figure 3). We place these patterns in the context of postglacial climate and sea-level fluctuations, including Meltwater Pulse 1a [MWP-1a, 14.6 – 14.3 ka, 48, 49], the Antarctic Cold Reversal [14.5 – 12.9 ka, 50, 51], the Younger Dryas event [12.9 – 11.7 ka, 52], Meltwater Pulse 1b [11.5 – 11.2 ka 53], and the 8.2 ka event [8.5 – 8.0 ka, 54]. In aggregate, we find no connection between MWP-1A and AIS thinning, an important perspective for comparison with individual site-based reconstructions that attribute their observations to this event [55–57]. Nearly all TCN-recorded thinning occurs after MWP-1a concludes (Figure 3a), and where thinning is ongoing, i.e. WSE, STaM/MB, EA, and AP, thinning does not expand or speed up. This finding does not preclude a sizable AIS contribution to MWP-1a [Fig. 3e 49, 58], as suggested by [59, 60], but does indicate that AIS thinning during MWP-1a must have occurred in areas or at elevations undocumented by TCN profiles. During the Antarctic Cold Reversal, when the Southern Ocean cooled [61] and AIS readvanced [51], AIS thickening would not be recorded by the PATR. However, our results do not show thinning starting in any region or an increase in thinning rate at sites where thinning is ongoing. The Younger Dryas, when AIS warmed [50, 62, 63], coincides with an expansion in thinning in the WSE and NTaM (Figure 2a, f): $>$ 50% of WSE and NTaM sites record thinning at over 0.1 cm/yr, and 10% thin at over 50 cm/yr (WSE) or 10 cm/yr (NTaM). This finding that has not been noted previously. During Meltwater Pulse 1b, during which WAIS accumulation [64] and Scotia Sea iceberg rafted debris increased [65], AIS thinning increases in the NTaM and EA, aligned with a hypothesized small but significant AIS contribution [66].

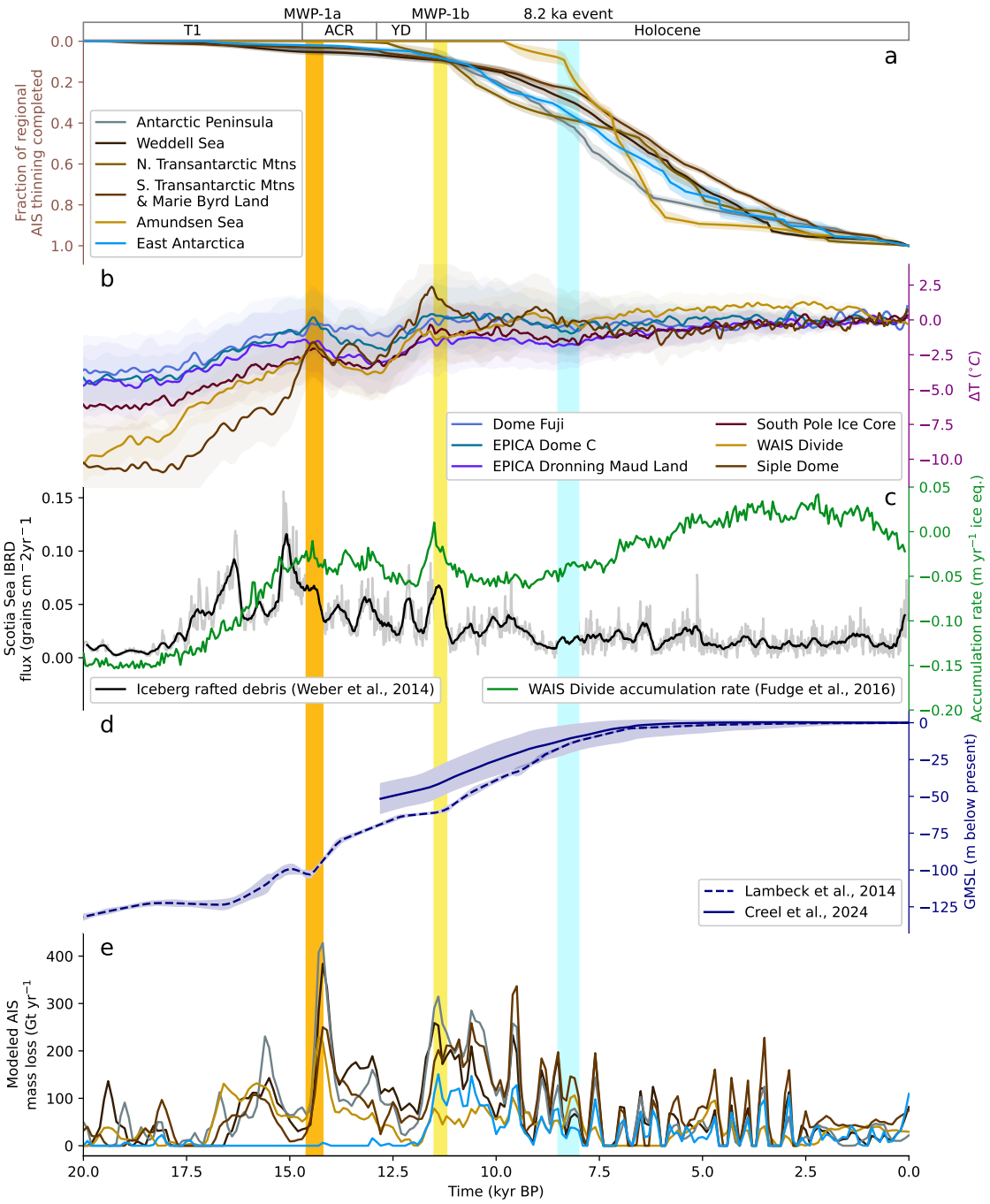


Fig. 3 Antarctic thinning in paleoclimate context. (a) Fraction of total thinning to occur at each Antarctic Ice Sheet (AIS) region. Regions correspond to blue polygons in Figure 1. Envelopes in all panels represent 95% credible intervals unless noted. **(b)** Antarctic surface temperature anomalies [67]. **(c)** Global mean sea level curves from [68] (dashed) and [12] (solid, envelope marks 90% credible interval). (d) Modeled sector-by-sector AIS mass loss [69].

The presence of a distinct thinning signal around the 8.2 ka event, when a Laurentide Ice Sheet proglacial lake outburst flood coincided with collapse of the Hudson Bay ice saddle [54, 70], is also apparent in our PATR (Figure 2). Widespread thinning initiates at ∼8.5-8.0 ka in every sector save the NTaM, with $>$ 50% of sites recording thinning faster than 0.1 cm/yr and 35% of sites recording thinning faster than 1 cm/yr. This thinning reduces in rate and extent by ∼7.5 ka in the WSE, EA, and ASE, and continues further into the mid-Holocene in STaM/MB. Multiple mechanisms could have driven an Antarctic response to the 8.2 ka event. Hudson Bay ice saddle melt and proglacial lake discharge likely warmed the Southern Ocean [70–73] through a bipolar seesaw effect [36, 74], as evidenced by concurrent South Atlantic sea-surface temperatures warming [75], South America growing wetter[76], and the South American Monsoon strengthening[77]. Southern Ocean warming could have increased AIS basal ice shelf melt [78, 79], which would help explain rapid Antarctic retreat during this interval [80–82]. Solid Earth

teleconnections also would invite an AIS response due to Antarctic sensitivity to Northern Hemisphere sea-level forcing [40, 83].

After the 8.2 ka event, thinning across Antarctica continues, tapering up to the Common Era (last 2000 years). This tapering is likely explained by a combination of Earth system drivers and modeling assumptions. Climatically, Laurentide and Eurasian Ice sheet demise by ∼6 ka [84] and GMSL reaching present levels between ∼6 and 4 ka [Figure 5c, 12, 68], reduced sea-level forcing of AIS to that attributable to mid-Holocene Greenland Ice Sheet retreat and readvance [85] plus ongoing glacial isostatic adjustment[21, 86]. Ocean forcing likely encouraged Holocene AIS thinning through upwelling of circumpolar deep water onto the continental shelf [87–89].

The Common Era tapering may also be an artifact of our assumptions. In assuming monotonic thinning, the PATR cannot address mid- to late-Holocene time gaps or low-elevation scatter that could be a sign of thinning/rethickening associated with Holocene readvance. Nevertheless, although TCN methods from exposed surfaces alone cannot capture rethickening, our observations of minimal Common Era AIS thinning are consistent with the abundant evidence for AIS readvance during the late Holocene from subglacial records [90–93]. This readvance likely overrode potentially widespread mid-late Holocene TCN evidence for a smaller-than-present AIS [94].

4 Comparing past to future Antarctic thinning

The continuous rates of the PATR enable us the novel opportunity to place TCN data into a comparable framework to modern observations such that we can compare past thinning to modern and projected rates. This comparison cannot be made directly at TCN thinning profile locations, as ice no longer covers these sites. Instead, it must be done by comparison to nearby ice streams whose dynamics drove thinning at the TCN sites [95]. We identify these TCN site-adjacent ice streams using InSAR-based present-day ice velocity maps [96]. We then sample thinning rates from the ICESat-2 observational record (2019-2025)[3]; ISMIP-6 projections to 2100 [4] under low and very emissions scenarios (SSP1-2.6, RCP8.5 / SSP5-8.5, respectively); and ISMIP-6 projections to 2300 that employ high emissions to 2100 then either repeat 2100 climatic forcing to 2300 or allow high emission forcing to continue to 2300 [5]. We next compare average rates across the full 6 year ICESat-2 record to maximum decadal rates from PATR and the ISMIP-6 ensembles (Fig. 4). We finally assess the dependence of maximum thinning rates on timescales of observation, providing additional paleo-perspective in this assessment by including modeled postglacial thinning rates from the Parallel Ice Sheet Model [1], which we also sample at TCN site-adjacent ice streams (Fig. 5b).

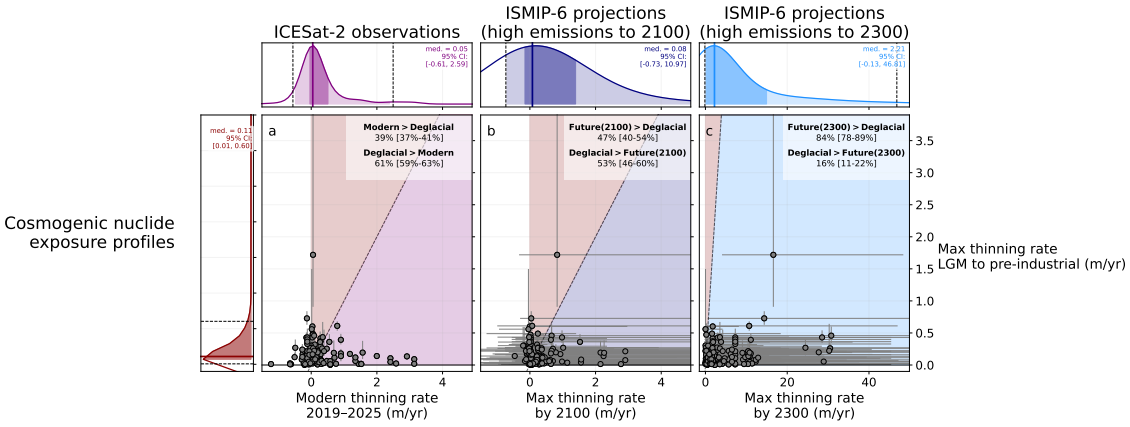


Fig. 4 Site-by-site comparison of past to modern and future local decadal ice thinning rates. (a) Maximum postglacial ice thinning rates, as estimated from cosmogenic exposure profiles, versus maximum modern (2019 – 2025) rates derived from ICESat-2 observations of ice streams near exposure profiles; **(b)** Maximum postglacial decadal thinning rates versus maximum 21st century ice thinning rates under a high emissions scenario (RCP8.5/SSP5-8.5). Future projections are from ISMIP6 ensemble members [4] sampled at ice streams near exposure profiles. **(c)** As in (b), but for the ISMIP6 ensemble extended to 2300 [5]. Marginal plots are thinning rate distributions from cosmogenic data (red), ICESat-2 observations (light purple), and ISMIP6 projections to 2100 (dark purple) and 2300 (blue). Dashed lines represent equality between past and present/future rates.

Decadal postglacial thinning rates have a median value of 0.11 m/yr (0.01 – 0.60 m/yr, 95% credible interval; all reported values are medians with 95% credible intervals unless otherwise noted); the range truncates at zero because TCN records from exposed archives are not interpreted to record thickening.

Modern ice streams adjacent to these profiles thinned from 2019 to 2025 at 0.05 m/yr (-0.61 – 2.59 m/yr, Fig. 4a). Under very high emissions, ISMIP-6 thinning projections to 2100 at these ice streams reach 0.08 m/yr (-0.73 – 10.97 m/yr, Fig. 4b), a maximum rate that remains virtually unchanged if high emissions are repeated at 2100 levels until 2300 (0.07 m/yr, -0.34 – 9.42 m/yr, Supplementary Fig. **??**c); with low emissions to 2100, future thinning rates reach 0.06 m/year (-0.71 – 5.29 m/yr, Supplementary Fig. **??**b). If very high emissions are sustained to 2300, maximum projected ISMIP-6 thinning rates increase to 2.21 m/yr (-0.13 – 46.91 m/yr, Fig. 4c). Considering only sites with net ice thinning in the modern and future, and sampling from the distributions on past and future thinning, we find that maximum postglacial thinning is 61% (59 - 63%) likely to be greater than modern thinning and 53% (46 - 60%) likely to be greater than maximum projected thinning by 2100 under very high emissions. However, past rates are only 16% (11 - 22%) likely to be greater than maximum thinning by 2300 if high emissions continue to 2300 (Figure 4)—a decrease in likelihood that is driven by forcing between 2100 and 2300.

5 Timescale dependence of thinning rates

The rates at which we measure ice sheets thinning depend on the timescale over which thinning is observed. This timescale dependence is guaranteed by the many processes that simultaneously influence ice thinning (Fig. 5a). At seasonal to annual timescales, Antarctic ice thinning is influenced by a combination of ocean forcing via ice shelf basal melt and buttressing loss [97] as well as atmospheric forcing via firn compaction and surface mass balance fluctuations [98]. At annual to multidecadal timescales, atmospheric and oceanic forcing are joined by grounded ice dynamics such as ice stream acceleration and draw-down [99]. And at decadal to millennial timescales, thinning responds to grounding line migration processes such as marine ice sheet instability [100] and marine ice cliff instability [101] as well as solid Earth sea-level feedbacks [42].

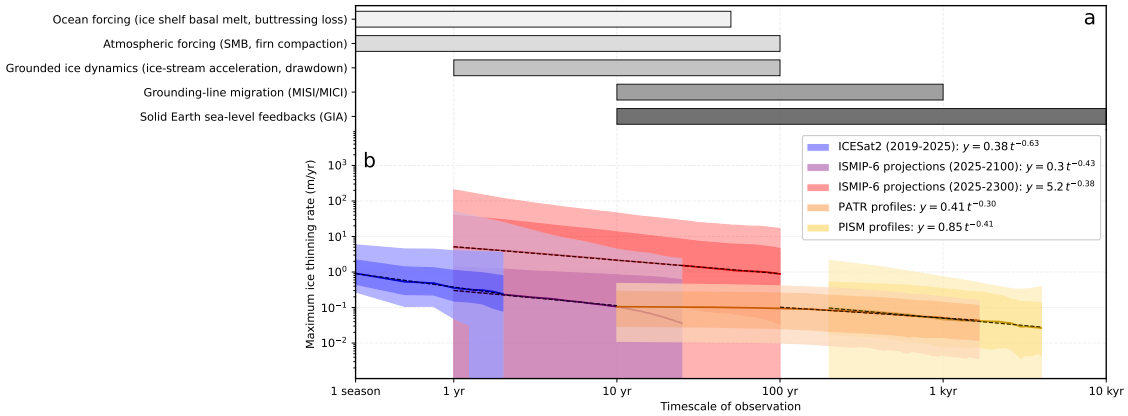


Fig. 5 Dependence of ice thinning rates on timescales of observation. (a) Timescales of influence for processes affecting Antarctic Ice Sheet mass loss. (b) Maximum thinning rates are shown as a function of timescale for past, modern, and future thinning estimates. Past estimates include terrestrial cosmogenic nuclide (TCN) exposure age profiles (purple, this study) and postglacial thinning profiles modeled using the Parallel Ice Sheet Model (PISM, gray envelope,[1]). Modern estimates are from ICESat-2 observations (red, [3]). Future projections are from ISMIP-6 simulations for a high emissions scenario sustained to 2300 (orange, [5]). PISM, ICESat-2, and ISMIP-6 data are sampled at ice stream centers near TCN exposure profiles. Dashed black lines (also shown in equation form in figure legend) mark best-fitting power law relationship; TCN rates over 10 to 100 yr window, and ISMIP-6 simulations to 2100 [4] for periods from 10 to 30 years, are not fit with power law curves. See methods for more details.

This process multiplicity is mirrored by the empirical timescale dependences of maximum rates of Antarctic ice sheet thinning (Fig. 5b). The time dependence of Antarctic thinning rates is well characterized with a power law relationship of the form $y(t) = a\left(\frac{t}{t_0}\right)^{-p}$, where t is the timescale of averaging; t_0 is the reference timescale, set to 1 year for all datasets; a is the maximum thinning-rate magnitude at a one-year timescale, hereafter termed 'amplitude', and p is the scale dependence, hereafter 'persistence'. Taken broadly, p values can be interpreted as indicative of process—larger p values indicates that thinning is dominated by episodic variability rather than sustained forcing; smaller p values suggest that high thinning rates persist even when averaged over decades to centuries—while a values reflect the overall amplitude of thinning but are process-agnostic. We quantify the time dependence of maximum Antarctic thinning rates for TCN, ICESat-2, and ISMIP-6 datasets, then fit the medians of the resulting distributions with power law equations (see Methods section 7.7 and Figure 5 legend).

Antarctic thinning rate datasets span a range of power law amplitudes and persistences. Whereas maximum thinning rates in the observed past (TCN), modern (ICESat-2), and projected 21st century (ISMIP-6) are best fit by amplitudes of 0.3–0.4, projected maximum future rates by 2300 are best fit with an amplitude of 5.2, indicating a systemic increase in thinning intensity across timescales. Higher amplitudes for PISM profiles relative to TCN profiles over the same timescales and periods (0.85 versus 0.41 over 200 to 1000 year averaging intervals) may indicate that PISM simulations are not capturing the magnitude of postglacial AIS thinning. By contrast, identical best-fit amplitudes for the two observational thinning datasets (TCN and ICESat-2) builds confidence that the PATR framework used to calculate centennial to millennial-scale thinning rates resides on the same spectrum as the higher frequency observational record and may reflect similar processes driving thinning. Persistence values follow an opposite pattern with similar interpretation. For model simulations of both paleo (PISM) and future (ISMIP-6) scenarios, persistence values are nearly identical (-0.38 to -0.43), suggesting that ice models on both timescales are simulating thinning patterns dominated by the same model processes. By contrast, observed persistence values are substantially different between the ICESat-2 and TCN records (-0.30 versus -0.63), underscoring how different the processes driving seasonal- to interannual thinning are from those driving thinning over centuries to millennia.

The timescale-dependence analysis also sheds light on the limitations of the PATR. First, maximum TCN thinning rates are largely invariant at sub-centennial timescales (Fig. 5b), indicating that TCN data likely capture maximal centennial- to millennial-scale ice thinning more accurately than decadal scale maxima. This occurs due to (1) TCN temporal uncertainties, (2) data sparcity such that it is unlikely that any TCN profile is composed of samples that record the exact moment ice retreated from a site, and (3) the twice differentiable nature of the statistical tool we use, which prioritizes smoothness over abrupt change. Second, ice streams thin faster than stream margins [102]: if past, present, and future thinning rates were identical, modern and future rates sampled from ice-stream centers should exceed TCN-derived rates from stream margins. These structural features indicate that the PATR rates should be considered minimum estimates, and that our past-to-future comparisons are therefore likely biased towards underestimating the likelihood that past rates are greater than projected future rates.

6 Implications for future Antarctic change

That past rates of AIS thinning rival 21st century rates but are exceeded by rates of thinning to 2300 under sustained high emissions adds a new dimension to the consideration of AIS tipping points. Rates of future AIS mass loss, which have received considerable attention, are projected to lag decades to centuries behind the onset of strong temperature forcing, in part due to the time it takes warm ocean water to destabilize AIS ice shelves, thereby increasing discharge, accelerating flow, and promoting grounding line retreat [103]. Rates of future AIS thinning or terrestrial retreat have received less scrutiny. For instance, the time delay between future grounding line retreat and upstream dynamic thinning on Antarctic nunataks remains unconstrained.

This lacuna may have persisted because of historical differences in perceived importance between AIS mass loss and thinning. Sea-level rise caused by with AIS mass loss will impact the large fraction of humanity living in coastal zones. By contrast, AIS thinning will mostly impact which areas of the Antarctic continental surface become ice-free in coming centuries. Until recently, future Antarctic surface exposure was poorly understood and considered a matter of little importance. However, recent extension of Antarctic projections to 2300 and beyond [5] has enabled detailed mapping of projected Antarctic exposure, which shows that under high emissions, ~120,000 km^2 of land is projected to emerge by 2300 [104]. This mapping has focused international attention on the surface that future thinning will soon expose. The implications of future thinning and the exposure it will bring are legion. Ice thinning will trigger exfiltration that may accelerate AIS mass loss through subglacial groundwater discharge [105]. Surface exposure will expose new ecosystems, driving biological invasions that may tip Antarctica into the pattern of rising species extinction observed on higher latitude continents [106, 107]. Exposure will also open Antarctica to expanded human exploitation, including through tourism [108, 109], habitation [110], ship traffic [111], and critical mineral extraction [104].

Antarctic emergence will be driven by 200–300 m of ice thinning [104], a amount similar to thinning amounts between LGM and today. However, future thinning will happen an order of magnitude faster than past thinning (Figure 5). In this light, understanding what drives local AIS thinning—including the physical processes acting on different timescales and success (or shortcomings) of models that project future thinning—becomes a matter of critical importance. Our results indicate that existing ice models are likely underestimating the processes driving ice sheet thinning on decadal to centennial timescales,

which indicates that AIS thinning over the coming centuries may occur faster than currently projected—a likelihood that international negotiations over the future of Antarctica [112] will need to take into account.

7 Methods

7.1 Data constraints on Antarctic thinning

TCN exposure dating in glacial geologic environments involves determining the length of time since a rock sample was last covered by ice [113]. Sample age is estimated by dividing the measured concentration of a nuclide by its production rate. A cosmogenic nuclide's production rate is primarily a function of latitude and altitude [114, 115], with additional effects from atmospheric pressure, magnetic field characteristics, and time [116–118]. As the state of knowledge about these factors evolves rapidly, the TCN community has routed (re)calibration through a centralized online calculator [119] and data management platform called the Informal Cosmogenic-nuclide Exposure-age Database (ICE-D; [19]). We use exposure age data from ICE-D's Antarctic database (https://version2.ice-d.org/antarctica/, accessed 06/2024 – 08/2024). The database combines measurements made on minerals of trace nuclides such as beryllium-10 (^{10}Be) or aluminum-26 (^{26}Al) with sample metadata including sample elevation, location, and physical characteristics like density and chemistry.

We screen exposure age data according to several criteria. First, for samples dated with both in situ ^{14}C and $^{10}Be/^{26}Al$, if the in situ ^{14}C age is younger than the $^{10}Be/^{26}Al$ age(s), we treat the in situ ^{14}C age as the true age of the sample unless authors specifically argue otherwise. Such a scenario can arise if a glacial period is not long enough for longer-lived nuclides ($^{10}Be/^{26}Al$) to decay back to baseline, resulting in a non-zero starting point during deglaciation—a phenomenon referred to as inheritance. In surfaces characterized by inheritance, the short half-life of in situ ^{14}C (5.7 kyr) enables us to decipher the true postglacial exposure age [120, 121]. If the in situ ^{14}C age is older than the $^{10}Be/^{26}Al$ age(s), we take the ^{10}Be age as the true age. Second, samples older than Holocene age (11.7 - 0 ka) that have a lower elevation than the highest Holocene sample are likely contaminated by inheritance and cannot be used to model postglacial ice thinning. Third, samples that authors reject because of field evidence are not included. Fourth, ^{3}He isotope and ^{36}Cl isotope dates reported in ICE-D are not included, as these data are considered of lower quality than TCN $^{10}Be/^{26}Al/^{14}C$ data (e.g. [32]). For samples that pass these criteria, and for which there are multiple samples at the same elevation at a single site, we assess the concordance of the data. If ^{10}Be and ^{26}Al ages overlap within 2σ internal uncertainties, we take the weighted mean of $^{10}Be/^{26}Al$ ages. If $^{10}Be/^{26}Al$ ages do not overlap within uncertainties, we assume that the ^{10}Be age is the true age and take the weighted mean of ^{10}Be-dated samples. In calculating weighted means and associated uncertainties, we employ an inverse-variance weighted mean. We define weights:

$$w_i = \frac{1}{\sigma_i^2}$$

We employ these weights to compute a combined age estimate,

$$\hat{\mu} = \frac{\sum_{i=1}^{n} w_i \mu_i}{\sum_{i=1}^{n} w_i},$$

and assess a 1σ uncertainty on the combined mean age of:

$$\hat{\sigma} = \sqrt{\frac{1}{\sum_{i=1}^{n} w_i}}.$$

We explore the importance for our results of this and subsequent modeling choices in Sections 7.2, 7.3, and 7.4.

We grouped exposure ages into individual transects following the 'dipstick' method (e.g. [14]; hereafter referred to as 'sites') based on the original publications as well as additional metadata in ICE-D. We split data into sites with as much granularity as possible, at times partitioning multiple dipstick profiles collected from a single mountain range into distinct sites. We employ this granular partitioning on the principle that local environmental conditions can lead exposure ages to differ by hundreds to thousands of years across short spatial scales due to factors such as exposure to sunlight, katabatic wind scouring, ice flow direction, and substrate roughness [122].

Beyond TCN data, we also include thinning constraints from radiocarbon dates on subfossil lacustrine cyanobacteria from the Lake Wellman region, Ross Sea Embayment [33], and an ice core record from

the Skytrain Ice Rise, Weddell Sea Embayment [34]. The radiocarbon data, from sediments preserved beneath lake-ice boulder pavements and glacial erratics, record Hatherton glacier thickening from 13 to 9.5 ka—which we do not simulate—then thinning until 2.8 ka. The Skytrain Ice Rise constraints employ total air content and $\delta^{18}O$ to estimate that local surface elevation lowered ∼450 m between 8.2 and 8.0 ka.

7.2 Exposure age uncertainty quantification

Exposure age data have uncertainties in elevation and age, of which some are commonly reported, others are typically omitted. We assess vertical and age uncertainties from a variety of sources and test the sensitivity of our results to modeling choices.

Exposure age calculations follow the V3 exposure age calculator in ICE-D [119]. Required information include sample latitude, longitude, elevation, thickness, density, shielding correction, erosion rate, nuclide concentrations, and uncertainties in nuclide concentrations. Shielding correction accounts for the fraction of a sample's nuclide production that is prevented from occurring because of surface slope angle and/or occluded horizons; erosion rate is inferred from independent evidence such as presence or absence of scour marks; nuclide concentrations (atoms g^{-1}) refers to the laboratory-measured ^{10}Be and/or ^{26}Al concentrations in quartz in the sample. Uncertainties in exposure age calculations are generally categorized into internal uncertainty—chiefly analytical uncertainties in nuclide concentration measurements, including blank uncertainty, nuclide concentration measurement uncertainty, and AMS measurement uncertainty—and external uncertainty, which includes uncertainty in reference nuclide production rate for spallation and by muons. Use of internal uncertainties is sufficient when comparing ages at a single site. External uncertainties are appropriate when comparing exposure ages from separate locations and/or from other dating techniques [119]. We use external uncertainties as reported in ICE-D.

Exposure age elevation E, measured in meters above sea level, is reported for every exposure age, as it is required for age determination. Techniques for determining exposure age sample elevations include differential GNSS; absolute GNSS; inference from topographic maps; inference from satellite-derived digital elevational maps; and leveling. Some Antarctic exposure age studies report both the method of elevational measurement and the uncertainty associated with that measurement (e.g. [23]). For those studies, we use elevational uncertainties as reported. For all other studies, we follow the sliding elevational uncertainty protocol of [123] and assign samples normally distributed vertical uncertainties equal to the larger of 2% of their absolute elevation and 5 m:

$$\sigma_E = max(5, \frac{E}{50}) \tag{1}$$

We justify this choice in two ways. First, rates of thinning are determined relative to present ice height, not present sea level, which introduces a second uncertain elevational measurement. Second, while ice elevation is typically reported in meters above sea level, a single value is commonly reported for a site even if data at that site span multiple kilometers in along-flow direction. [56] report this difference in relative elevation as up to 7 meters at Gemini Nunataks, 166 meters at Mt. Hope, and 73 meters at Mt. Rigby. We attempt to minimize relative elevation uncertainty by subdividing exposure age data into individual transects. Nevertheless, it is unlikely that 5 meters of elevational uncertainty grossly overestimates vertical data uncertainties.

7.3 Penalized cubic spline algorithm

We design and employ a statistical tool in Python to fit surface-exposure data. This tool bears similarities to, but is distinct from, the iceTEA tool [124]. We divide surface exposure data into s sites, each with n exposure data with elevations $E_0, E_1, ..., E_n$ with normally distributed uncertainties $\sigma_{E_0}, \sigma_{E_1}, ..., \sigma_{E_n}$ and ages $A_0, A_1, ..., A_n$ with normally distributed uncertainties $\sigma_{A_o}, \sigma_{A_1}, ..., \sigma_{A_n}$. Ice elevation at site s is estimated using a penalized univariate cubic B-spline $f(x)$, defined as the linear combination of K control points c_i and piecewise cubic polynomial basis functions $B_i(x)$:

$$f(x) = \sum_{i=0}^{K} c_i B_{i,3}(x) \tag{2}$$

where B-spline basis functions satisfy $\sum_{i=0}^{n} B_i(x) = 1$. Cubic basis functions $B_{i,3}(x)$ are defined recursively:

$$B_{i,3}(x) = \frac{x - \xi_i}{\xi_{i+4} - \xi_i} B_{i,2}(x) + \frac{\xi_{i+4} - x}{\xi_{i+4} - \xi_{i+1}} B_{i+1,2}(x) \tag{3}$$

where $\xi_i, \xi_{i+1}, \ldots, \xi_{i+4}$ are knot locations and $B_{i,2}(x)$ is a quadratic basis function, which is built from linear B-splines, which in turn are built from degree 0 basis functions:

$$B_{i,0}(x) = \begin{cases} 1, & \text{if } \xi_i \leq x < \xi_{i+1}, \\ 0, & \text{otherwise.} \end{cases} \tag{4}$$

The penalized univariate cubic splines used here can be thought of as collections of flexible curves in age–elevation space whose curvature is determined by the cubic degree of the polynomial forming them, the likelihood function penalizing the curves' vertical position, the number of control points K, which determine the spline's shape, and the 'knots' m, which govern where and how polynomial segments join. The number of knots helps to define the flexibility of the spline: more knots allow for more complexity while fewer knots produce simpler curves. For each spline model, we specify that $m = n + 3$, i.e. we use three more knots than exposure age data. We follow standard practice in setting $K = n + 4$, and space knots evenly between the lowest and highest exposure ages.

Beyond knot number, the chief control on spline shape is the likelihood function applied to control the spline's smoothness. We construct our likelihood function with multiple terms that penalize the spline fit according to assumptions standard in Antarctic exposure age dating. We first assume that exposure age data accurately represent the times and elevations at which bedrock was exposed, and create a goodness-of-fit penalty L_g for deviations from the data using a weighted residual sum of squares formulation:

$$L_g = -\frac{1}{2} \sum_{j=0}^{n} \left(\frac{(A_j - \hat{A}_j)^2}{\sigma_{A_j}^2} + \frac{(E_j - \hat{E}_j)^2}{\sigma_{E_j}^2} \right). \tag{5}$$

where $\hat{A}_j$ and $\hat{E}_j$ are the model-predicted age and elevation, respectively. We further penalize the spline if it fails to pass higher and younger than each datum:

$$L_y = -\sum_{j=0}^{n} \left(\max\left(0,\ \frac{E_j - \hat{E}_j}{\sigma_{E_j}^2} + \frac{A_j - \min(A)}{\sigma_{A_i} \max(A) - \min(A)} \right) \right)^2 R_y. \tag{6}$$

where $\frac{E_j - \hat{E}_j}{2\sigma_{E_j}}$ is the elevation difference scaled by elevation uncertainty, $\frac{A_j - \min(A)}{\sigma_{A_i}^2 \max(A) - \min(A)}$ is the age difference scaled to a unit interval, and R_y is a scaling factor. This penalty enforces a standard assumption in the TCN community [14, 17, 122] and helps reduce thinning histories that pass below or older than TCN data, which occurred when Equation 5 alone constrained the model. We next enforce that ice thinned uniformly from local Last Glacial Maximum (LGM) to present ice surface by penalizing the spline to enforce that the coefficients are non-decreasing:

$$L_u = -\sum_{j=0}^{K-1} \left(\max(0,\ c_j - c_{j+1})\right)^2 R_u. \tag{7}$$

where R_u is a scaling factor. We additionally penalize the spline to ensure that the spline's highest elevation occurs at the age corresponding to the highest observed elevation:

$$L_h = -\left(\hat{E}_t - \max(E)\right)^2 R_h. \tag{8}$$

where $\hat{E}_t$ is the age of the sample with the highest elevation and R_h is a scaling factor. We further penalize the model to prescribe that the lowest spline elevation occurs at the youngest age:

$$L_b = -\left(\hat{E}_y - \min(E)\right)^2 R_b. \tag{9}$$

where $\hat{E}_y$ is the elevation of the youngest sample and R_b is a scaling factor. Equations 8 and 9, which reinforce Equation 5, were found necessary to produce realistic thinning profiles at sites where data constraining upper and lower thinning bounds are scarce.

These terms are combined into an overall likelihood function $L(\mathbf{c})$:

$$L(\mathbf{c}) = L_g + L_y + L_u + L_h + L_b. \tag{10}$$

Scaling factors R_y, R_u, R_h are introduced to weight the likelihood function such that it correctly enforces that the spline (1) reach the highest datapoint at that datapoint's age, (2) increase uniformly, and (3) pass younger and higher than the exposure data. Initially set to unity, (R_y, R_u, R_h) were then experimentally increased by factors of 10 until proper spline behavior was produced; the sensitivity of the model to these weights is investigated in Section 7.4.

We next find a posterior distribution on control point $c = (c_0, c_1, \ldots, c_K)$ that best fits the observed data given the model's functional form and the penalties we prescribe. For this optimization we employ a Metropolis–Hastings algorithm with a Gibbs sampler. For each control point c_j, we draw a new value c'_j from a normal distribution centered on c_j:

$$c'_j = c_j + \epsilon, \qquad \epsilon \sim \mathcal{N}(0, \sigma_m^2). \tag{10}$$

where σ_m is the proposal scale, chosen to be 10 meters based on the range of data elevations relative to present-day ice surface (C9). The log likelihood of current and proposed control points—$L(c_j)$ vs. $L(c'_j)$—is computed, then an acceptance ratio r is computed:

$$r = \frac{P(n \mid c'_j)}{P(n \mid c_j)} = e^{L(c'_j) - L(c_j)}. \tag{11}$$

We accept the proposed control point and update c_j to be c'_j if r exceeds a number u drawn from a uniform random distribution $[0, 1]$. This process is repeated for each control point in turn, and 2000 coefficient samples are stored after a 1000 sample burn-in. We also apply this algorithm to fit the radiocarbon-dated lake sediment records from Lake Wellman. For the Skytrain Ice Rise thinning data, we reduce noise and extract long term trends in the Skytrain elevation curves by fitting the records with segmented linear regression, then smoothing the resulting regression with a univariate spline at visually identified breakpoints (Supplemental Fig. **??**).

7.4 Sensitivity Tests

We perform sensitivity analysis to test the robustness of our results to modeling choices. These choices include using the in situ carbon age if that age is younger than Be/Al ages, otherwise taking the weighted mean of Be/Al exposure ages from samples at a single stratigraphic level when Be/Al are concordant, and the mean of only Be exposure ages when Be/Al are not concordant (C1); placing breakpoints for piecewise linear regression of Skytrain ice rise observations by visual inspection (C2); using external exposure age uncertainties (C3); assessing sample vertical uncertainties as the greater of 5 m or 2% of a sample's elevation above mean sea level (C4); equating the number of spline knots to 3 more than the number of data (C5); using penalty terms L_y, L_u, L_h, L_b with scaling factors R_y, R_u, and R_h (C6, C7, C8, C9); setting the Metropolis–Hastings proposal scale m to 10 m (C10); and to accept 1000 control point samples during Gibbs sampling after a 1000 sample burn-in (C11). We perform sensitivity tests by varying each parameter in turn.

We summarize our sensitivity tests in Supplementary Table 1, and replicate Figure 2 with each test (Supplementary Figs. 6 - 35) to demonstrate the importance of each choice. We additionally replicate Figure 3a region-by-region using the sensitivity test results (Supplementary Figure **??**), and show the difference between the PATR using our preferred parameters and each sensitivity test in Supplementary Figures **??** - **??**.

These tests reveal that choice of parameterization impacts the fraction of regional thinning completed at a given timestep differently in each region. Lowest impacts occur in StAM/MB, WS, and EA, where differences are generally less than ∼10% across all tests. On the AP and in the NTaM, differences reach 20% in the mid-Holocene (7.5 ka, AP; ∼4-5 ka, NTaM) but otherwise are generally less than 10%. Largest differences occur in the ASE, where multiple sensitivity tests lead to differences of 20%, likely because overall ASE thinning occurs within a much shorter time window (∼2.5 kyr) than other regions. Overall, largest differences occurring during the early- to mid- Holocene (12–4 ka), when thinning is most widespread (Supplementary Figure **??**). In addition to quantifying structural uncertainties in the PATR, the sensitivity tests reveal the robustness of the overall results to modeling choices: parameterization does not change the qualitative pattern of thinning within a single region or the first-order relative timing of thinning between regions (Supplementary Figure **??**). This consistency suggests that when considered at regional- to pan-Antarctic scale, the postglacial thinning rates we simulate—and the links we suggest to global climate events—are robust to modeling choices.

Table 1 Sensitivity tests employed to determine importance of modeling choices in posterior results. Stars indicate parameters employed in main study. *X* denotes choice used in main study; *a, b, c* denote sensitivity tests. Note that C2 did not have a qualitative impact on our results so was not included in further analysis.

Modeling choice	Sensitivity test
C1*X*, b, c	Weighted mean if concordant, Be if not concordant*; youngest age at stratigraphic level; weighted mean
C2	Varying Skytrain regression breakpoints
C3	Using external* vs. internal exposure age uncertainties
C4a, *X*, b, c	$\max(2, E/100)$; $\max(5, E/50)$*; $\max(7.5, E/33)$; $\max(10, E/25)$
C5a, *X*, b, c	$m = n + 1$; $n + 3$*; $n + 5$; $n + 10$
C6a, *X*, b, c	$R_y = 0$; $R_y = 1$*; $R_y = 10$; $R_y = 100$
C7a, *X*, b, c	$R_u = 1$; $R_u = 10$*; $R_u = 100$; $R_u = 1000$
C8a, *X*, b, c	$R_h = 0$; $R_h = 1$*; $R_h = 10$; $R_h = 100$
C9a, *X*, b, c	$R_b = 0$; $R_b = 1$*; $R_b = 10$; $R_b = 100$
C10a, *X*, b, c	$\sigma_m = 1$; $\sigma_m = 10$*; $\sigma_m = 50$; $\sigma_m = 100$
C11a, b, *X*, c	Samples = 500; 1000*; 2000; 3000

7.5 Regional thinning rate aggregation

Once fit with statistical models, thinning profiles at each site are aggregated regionally (Figure 1 boxes). In this aggregation we account for spatial clustering using Density-Based Spatial Clustering of Applications with Noise, an unsupervised machine learning technique commonly used in the data mining community because of its skill in identifying arbitrarily-shaped clusters (DBSCAN, [125]). We identify clusters based on a maximum distance of 0.5 degrees that two sites can be separated and still be considered in the same cluster—a threshold that meets the requirements that sites with broadly common exposure histories group into the same cluster, while sites more distant receive their own cluster—and weigh sites within each cluster such that all clusters receive equal weight.

7.6 Comparing past to future rates

For each paleo-thinning profile, we first locate the nearest ice stream by identify the fastest ice velocity within 10 km using MEaSUREs V2, an Antarctic ice velocity product at 450 m resolution based on Interferometric Synthetic-Aperture Radar (InSAR) data collected between 1996 and 2016 [96]. We then determine modern (2019 - 2025) ice thinning rates at that location of fast ice motion using ICESat-2, a NASA satellite altimetry mission with 3-month temporal resolution that is used here at 1 km spatial resolution [3]. Comparison of modern ice stream thinning rates to past TCN thinning rates is appropriate because thinning at ice stream centers governs flank thinning that TCN transects record [126]. To determine projected future Antarctic ice thinning, we extract thinning profiles at the same ice stream locations from the ISMIP-6 ensemble, which are at annual timescale [4]. For additional paleo-perspective, we include simulated ice thicknesses from the postglacial Antarctic Ice Sheet ensemble of [1], which we also sample at the ice stream locations.

7.7 Dependence of thinning rates on timescales of observation

We seek to assess the dependence of pan-Antarctic thinning on timescale of observation. Let $H_{e,s}(t)$ be time-dependent thickness at site s for some ensemble member e (e.g. ISMIP-6 experiment, PATR posterior sample, etc.), sampled on a regular time grid $t_n = t_0\delta_t, n = 0, ..., N-1$. We define an integer stride $k \geq 1$, which represents physical duration $\Delta = k\delta t$, and an offset $j \in \{_{0,\ldots,k-1}\}$. We then define the strided series

$$H_{e,s}^{(k,j)}(m) \;:=\; H_{e,s}[j + mk], \qquad m = 0, 1, \ldots, M_{k,j} - 1, \tag{11}$$

where m is a list of start times and

$$M_{k,j} \;=\; \left\lfloor \frac{N - 1 - j}{k} \right\rfloor + 1 \tag{12}$$

is the number of terms. We then compute a rate on each strided interval with respect to time. Working in Python, we employ `xarray.differentiate`, which corresponds to finite differences divided by the time step. Outside of endpoint conventions, the centered-difference approximation employed by `xarray.differentiate` is

$$T_{e,s}^{(k,j)}[m] \;\approx\; -\frac{H_{e,s}^{(k,j)}[m+1] - H_{e,s}^{(k,j)}[m-1]}{2\,k\,\delta t}. \tag{13}$$

where thinning T is defined as a negative thickness change.

We then seek to derive a maximum thinning rate over start times and offsets. For each (e, s, k, j), we define the maximum thinning rate over start times (i.e., over m) and over offsets j to yield a stride-k extreme for ensemble member e at site s

$$M_{e,s}^{(k,j)} := \max_{m} \max_{j\in\{0,\ldots,k-1\}} \left(T_{e,s}^{(k,j)}[m]\right) \tag{14}$$

For each duration Δ, we compute quantiles across sites $s \in \mathcal{S}$ and ensemble members $e \in \mathcal{E}$:

$$Q_\alpha(\Delta) := \text{Quantile}_\alpha\Big(\{\, M_{e,s}^{(k)} : e \in \mathcal{E},\, s \in \mathcal{S} \,\}\Big), \qquad \Delta = k\,\delta t,\ \alpha \in (0,1). \tag{15}$$

Repeated across durations, this procedure yields quantile distributions for the time dependence of pan-Antarctic thinning.

7.8 Sensitivity of past-future comparison to non-linear thinning

To bolster confidence in our non-linear estimates of past thinning, we reproduce the analysis using a linear statistical thinning tool similar to past statistical treatments of TCN data using linear models [17, 23, 26, 124]. Since our goal is to assess maximum thinning rates in order to compare those rates to modern and future rates, we visually identify the rough onsets and terminations of rapid thinning at each site and truncate data at these boundaries. We then apply to these data orthogonal distance regression, a linear regression technique that accounts for uncertainties in both vertical and horizontal dimensions [127]. We quantify uncertainties by Monte Carlo sampling all data points from their Gaussian uncertainties 1000 times, repeating the regression on each draw. The resulting probabilistic linear rates are then compared to past to present and future AIS rates (Figure **??**).

Acknowledgments. The authors thank numerous colleagues for helpful discussions and feedback throughout the development of this study.

8 Algorithms, Program codes and Listings

All algorithms and program codes developed and used in this study are openly available for transparency and reproducibility. The complete source code, along with documentation and usage instructions, can be accessed at XXX.

Declarations

- **Funding:** The authors acknowledge a Woods Hole Postdoctoral Scholarship (RC), Texas A&M start up funding (RC), NSF award OPP-2303344 (RV), NSF-OAC 2513540 (ARH).
- **Conflict of interest/Competing interests:** The authors declare that they have no conflict of interest or competing interests.
- **Ethics approval and consent to participate:** Not applicable.
- **Consent for publication:** Not applicable.
- **Data availability:** All datasets used in this study are publicly available from the sources cited in the manuscript.
- **Materials availability:** Not applicable.
- **Code availability:** The algorithms and program codes used in this study are publicly available at .
- **Author contribution:** Conceptualization: R. Creel, R.V., R.H. Software: R. Creel Validation: R. Creel Formal analysis: R. Creel. Investigation: All authors, led by R. Creel Resources: R. Creel Writing - original draft: R. Creel, with input from R.V. and R.H. Writing - review and editing: all authors. Visualisation: R. Creel

References

[1] Albrecht, T., Winkelmann, R. & Levermann, A. Glacial-cycle simulations of the Antarctic Ice Sheet with the Parallel Ice Sheet Model (PISM) – Part 1: Boundary conditions and climatic forcing. *The Cryosphere* **14**, 599–632 (2020). URL https://www.the-cryosphere.net/14/599/2020/.

[2] Mas e Braga, M. *et al.* Nunataks as barriers to ice flow: implications for palaeo ice sheet reconstructions. *The Cryosphere* **15**, 4929–4947 (2021). URL https://tc.copernicus.org/articles/15/4929/2021/.

[3] Markus, T. *et al.* The Ice, Cloud, and land Elevation Satellite-2 (ICESat-2): Science requirements, concept, and implementation. *Remote Sensing of Environment* **190**, 260–273 (2017). URL https://www.sciencedirect.com/science/article/pii/S0034425716305089.

[4] Seroussi, H. *et al.* ISMIP6 Antarctica: a multi-model ensemble of the Antarctic ice sheet evolution over the 21st century. *The Cryosphere* **14**, 3033–3070 (2020). URL https://tc.copernicus.org/articles/14/3033/2020/.

[5] Seroussi, H. *et al.* Evolution of the Antarctic Ice Sheet Over the Next Three Centuries From an ISMIP6 Model Ensemble. *Earth's Future* **12**, e2024EF004561 (2024). URL https://onlinelibrary.wiley.com/doi/abs/10.1029/2024EF004561. _eprint: https://agupubs.onlinelibrary.wiley.com/doi/pdf/10.1029/2024EF004561.

[6] Noble, T. L. *et al.* The Sensitivity of the Antarctic Ice Sheet to a Changing Climate: Past, Present, and Future. *Reviews of Geophysics* **58**, e2019RG000663 (2020). URL https://onlinelibrary.wiley.com/doi/abs/10.1029/2019RG000663. _eprint: https://onlinelibrary.wiley.com/doi/pdf/10.1029/2019RG000663.

[7] Lecavalier, B. S. & Tarasov, L. A history-matching analysis of the Antarctic Ice Sheet since the Last Interglacial – Part 1: Ice sheet evolution. *The Cryosphere* **19**, 919–953 (2025). URL https://tc.copernicus.org/articles/19/919/2025/.

[8] Bentley, M. J. *et al.* A community-based geological reconstruction of Antarctic Ice Sheet deglaciation since the Last Glacial Maximum. *Quaternary Science Reviews* **100**, 1–9 (2014). URL https://www.sciencedirect.com/science/article/pii/S0277379114002546.

[9] Jouzel, J. *et al.* The two-step shape and timing of the last deglaciation in Antarctica. *Climate Dynamics* **11**, 151–161 (1995). URL https://doi.org/10.1007/BF00223498.

[10] Bodart, J. A. *et al.* High mid-Holocene accumulation rates over West Antarctica inferred from a pervasive ice-penetrating radar reflector. *The Cryosphere* **17**, 1497–1512 (2023). URL https://tc.copernicus.org/articles/17/1497/2023/.

[11] Whitehouse, P. L., Bentley, M. J., Milne, G. A., King, M. A. & Thomas, I. D. A new glacial isostatic adjustment model for Antarctica: calibrated and tested using observations of relative sea-level change and present-day uplift rates. *Geophysical Journal International* **190**, 1464–1482 (2012). URL https://doi.org/10.1111/j.1365-246X.2012.05557.x.

[12] Creel, R. C. *et al.* Global mean sea level likely higher than present during the holocene. *Nature Communications* **15**, 10731 (2024). URL https://www.nature.com/articles/s41467-024-54535-0.

[13] Schaefer, J. M. *et al.* Cosmogenic nuclide techniques. *Nature Reviews Methods Primers* **2**, 18 (2022). URL https://www.nature.com/articles/s43586-022-00096-9.

[14] Stone, J. O. *et al.* Holocene Deglaciation of Marie Byrd Land, West Antarctica. *Science* **299**, 99–102 (2003). URL https://www.science.org/doi/full/10.1126/science.1077998.

[15] Hein, C. J. *et al.* Coastal response to late-stage transgression and sea-level highstand. *Geological Society of America Bulletin* 22 (2014).

[16] Bentley, M. J. *et al.* Deglacial history of the Pensacola Mountains, Antarctica from glacial geomorphology and cosmogenic nuclide surface exposure dating. *Quaternary Science Reviews* **158**,

58–76 (2017). URL https://www.sciencedirect.com/science/article/pii/S027737911630378X.

[17] Small, D., Bentley, M. J., Jones, R. S., Pittard, M. L. & Whitehouse, P. L. Antarctic ice sheet palaeo-thinning rates from vertical transects of cosmogenic exposure ages. *Quaternary Science Reviews* **206**, 65–80 (2019). URL https://www.sciencedirect.com/science/article/pii/S0277379118307728.

[18] Spector, P. & Balco, G. Exposure-age data from across Antarctica reveal mid-Miocene establishment of polar desert climate. *Geology* **49**, 91–95 (2020). URL https://doi.org/10.1130/G47783.1.

[19] Balco, G. Technical note: A prototype transparent-middle-layer data management and analysis infrastructure for cosmogenic-nuclide exposure dating. *Geochronology* **2**, 169–175 (2020). URL https://gchron.copernicus.org/articles/2/169/2020/.

[20] Johnson, J. S. *et al.* Comparing Glacial-Geological Evidence and Model Simulations of Ice Sheet Change since the Last Glacial Period in the Amundsen Sea Sector of Antarctica. *Journal of Geophysical Research: Earth Surface* **126**, e2020JF005827 (2021). URL https://onlinelibrary.wiley.com/doi/abs/10.1029/2020JF005827. _eprint: https://onlinelibrary.wiley.com/doi/pdf/10.1029/2020JF005827.

[21] Suganuma, Y. *et al.* Regional sea-level highstand triggered Holocene ice sheet thinning across coastal Dronning Maud Land, East Antarctica. *Communications Earth & Environment* **3**, 1–11 (2022). URL https://www.nature.com/articles/s43247-022-00599-z.

[22] White, D. A. *et al.* Rapid ice sheet response to deglacial and Holocene paleoenvironmental changes in eastern Prydz Bay, East Antarctica. *Quaternary Science Reviews* **280**, 107401 (2022). URL https://www.sciencedirect.com/science/article/pii/S0277379122000324.

[23] Jones, R. S. *et al.* Rapid Holocene thinning of an East Antarctic outlet glacier driven by marine ice sheet instability. *Nature Communications* **6**, 8910 (2015). URL https://www.nature.com/articles/ncomms9910.

[24] Hein, A. S., Fogwill, C. J., Sugden, D. E. & Xu, S. Glacial/interglacial ice-stream stability in the Weddell Sea embayment, Antarctica. *Earth and Planetary Science Letters* **307**, 211–221 (2011). URL https://www.sciencedirect.com/science/article/pii/S0012821X11002536.

[25] Yamane, M. *et al.* The last deglacial history of Lützow-Holm Bay, East Antarctica. *Journal of Quaternary Science* **26**, 3–6 (2011). URL https://onlinelibrary.wiley.com/doi/abs/10.1002/jqs.1465. _eprint: https://onlinelibrary.wiley.com/doi/pdf/10.1002/jqs.1465.

[26] Johnson, J. S., Nichols, K. A., Goehring, B. M., Balco, G. & Schaefer, J. M. Abrupt mid-Holocene ice loss in the western Weddell Sea Embayment of Antarctica. *Earth and Planetary Science Letters* **518**, 127–135 (2019). URL https://www.sciencedirect.com/science/article/pii/S0012821X19302638.

[27] Johnson, J. S. *et al.* Review article: Existing and potential evidence for Holocene grounding line retreat and readvance in Antarctica. *The Cryosphere* **16**, 1543–1562 (2022). URL https://tc.copernicus.org/articles/16/1543/2022/.

[28] Roman, M. *et al.* Accelerated retreat of northern James Ross Island ice streams (Antarctic Peninsula) in the Early-Middle Holocene induced by buoyancy response to postglacial sea level rise. *Earth and Planetary Science Letters* **641**, 118803 (2024). URL https://www.sciencedirect.com/science/article/pii/S0012821X2400236X.

[29] Adams, J. R. *et al.* New ^{10}Be exposure ages improve Holocene ice sheet thinning history near the grounding line of Pope Glacier, Antarctica. *The Cryosphere* **16**, 4887–4905 (2022). URL https://tc.copernicus.org/articles/16/4887/2022/.

[30] Pittard, M. L., Whitehouse, P. L., Bentley, M. J. & Small, D. An ensemble of Antarctic deglacial simulations constrained by geological observations. *Quaternary Science Reviews* **298**, 107800

(2022). URL https://www.sciencedirect.com/science/article/pii/S0277379122004310.

[31] Halberstadt, A. R. W. & Balco, G. Antarctic ice sheet model comparison with uncurated geological constraints shows that higher spatial resolution improves deglacial reconstructions. *The Cryosphere* **20**, 931–961 (2026). URL https://tc.copernicus.org/articles/20/931/2026/.

[32] Balco, G., Stone, J. O., Sliwinski, M. G. & Todd, C. Features of the glacial history of the Transantarctic Mountains inferred from cosmogenic ^{26} Al, ^{10} Be and ^{21} Ne concentrations in bedrock surfaces. *Antarctic Science* **26**, 708–723 (2014). URL https://www.cambridge.org/core/product/identifier/S0954102014000261/type/journal_article.

[33] King, C., Hall, B., Hillebrand, T. & Stone, J. Delayed maximum and recession of an East Antarctic outlet glacier. *Geology* **48**, 630–634 (2020). URL https://doi.org/10.1130/G47297.1.

[34] Grieman, M. M. *et al.* Abrupt Holocene ice loss due to thinning and ungrounding in the Weddell Sea Embayment. *Nature Geoscience* **17**, 227–232 (2024). URL https://www.nature.com/articles/s41561-024-01375-8.

[35] Warrick, R. A. *et al.* in *Sea level rise* 257–282 (Cambridge University Press, 1990). URL https://research.manchester.ac.uk/en/publications/sea-level-rise/.

[36] Broecker, W. S. Paleocean circulation during the Last Deglaciation: A bipolar seesaw? *Paleoceanography* **13**, 119–121 (1998). URL https://onlinelibrary.wiley.com/doi/abs/10.1029/97PA03707. _eprint: https://onlinelibrary.wiley.com/doi/pdf/10.1029/97PA03707.

[37] Joughin, I., Alley, R. B. & Holland, D. M. Ice-Sheet Response to Oceanic Forcing. *Science* **338**, 1172–1176 (2012). URL https://www.science.org/doi/full/10.1126/science.1226481.

[38] Golledge, N. R., Fogwill, C. J., Mackintosh, A. N. & Buckley, K. M. Dynamics of the last glacial maximum Antarctic ice-sheet and its response to ocean forcing. *Proceedings of the National Academy of Sciences* **109**, 16052–16056 (2012). URL https://www.pnas.org/doi/abs/10.1073/pnas.1205385109.

[39] Bromwich, D. H., Chen, B., Hines, K. M. & Cullather, R. I. Global atmospheric responses to Antarctic forcing. *Annals of Glaciology* **27**, 521–527 (1998). URL https://www.cambridge.org/core/journals/annals-of-glaciology/article/global-atmospheric-responses-to-antarctic-forcing/1D5AA164DEC2D6CB61A6207DC4DD47CC.

[40] Gomez, N., Weber, M. E., Clark, P. U., Mitrovica, J. X. & Han, H. K. Antarctic ice dynamics amplified by Northern Hemisphere sea-level forcing. *Nature* **587**, 600–604 (2020). URL https://www.nature.com/articles/s41586-020-2916-2.

[41] Barletta, V. R. *et al.* Observed rapid bedrock uplift in Amundsen Sea Embayment promotes ice-sheet stability. *Science* **360**, 1335–1339 (2018). URL http://science.sciencemag.org/content/360/6395/1335.

[42] Whitehouse, P. L., Gomez, N., King, M. A. & Wiens, D. A. Solid Earth change and the evolution of the Antarctic Ice Sheet. *Nature Communications* **10**, 503 (2019). URL https://www.nature.com/articles/s41467-018-08068-y.

[43] Davis, P. E. D. *et al.* Variability in Basal Melting Beneath Pine Island Ice Shelf on Weekly to Monthly Timescales. *Journal of Geophysical Research: Oceans* **123**, 8655–8669 (2018). URL https://onlinelibrary.wiley.com/doi/abs/10.1029/2018JC014464. _eprint: https://agupubs.onlinelibrary.wiley.com/doi/pdf/10.1029/2018JC014464.

[44] Meur, E. L. & Huybrechts, P. A comparison of different ways of dealing with isostasy: examples from modelling the Antarctic ice sheet during the last glacial cycle. *Annals of Glaciology* **23**, 309–317 (1996). URL https://www.cambridge.org/core/journals/annals-of-glaciology/article/comparison-of-different-ways-of-dealing-with-isostasy-examples-from-modelling-the-antarctic-ice-sheet-during-the-55182CE55F12804620B93CCEE90BB0DD.

[45] Watanabe, O. *et al.* Homogeneous climate variability across East Antarctica over the past three glacial cycles. *Nature* **422**, 509–512 (2003). URL https://www.nature.com/articles/nature01525.

[46] Stokes, C. R. *et al.* Response of the East Antarctic Ice Sheet to past and future climate change. *Nature* **608**, 275–286 (2022). URL https://www.nature.com/articles/s41586-022-04946-0.

[47] Briggs, R. D. & Tarasov, L. How to evaluate model-derived deglaciation chronologies: a case study using Antarctica. *Quaternary Science Reviews* **63**, 109–127 (2013). URL http://www.sciencedirect.com/science/article/pii/S0277379112004921.

[48] Weaver, A. J., Saenko, O. A., Clark, P. U. & Mitrovica, J. X. Meltwater Pulse 1A from Antarctica as a Trigger of the Bølling-Allerød Warm Interval. *Science* **299**, 1709–1713 (2003). URL https://www.science.org/doi/full/10.1126/science.1081002.

[49] Coonin, A. N., Lau, H. C. P. & Coulson, S. Meltwater Pulse 1A sea-level-rise patterns explained by global cascade of ice loss. *Nature Geoscience* 1–6 (2025). URL https://www.nature.com/articles/s41561-025-01648-w.

[50] Jouzel, J. *et al.* in *The Last Deglaciation in Antarctica : Evidence for a "Younger Dryas" Type Climatic Event* .

[51] Baroni, C. *et al.* ANTARCTIC ICE SHEET RE-ADVANCE DURING THE ANTARCTIC COLD REVERSAL IDENTIFIED IN THE WESTERN ROSS SEA (2022). URL https://ricerca.ogs.it/handle/20.500.14083/17102. Accepted: 2023-04-17T11:58:30Z.

[52] Broecker, W. S. *et al.* Putting the Younger Dryas cold event into context. *Quaternary Science Reviews* **29**, 1078–1081 (2010). URL https://www.sciencedirect.com/science/article/pii/S027737911000051X.

[53] Abdul, N. A., Mortlock, R. A., Wright, J. D. & Fairbanks, R. G. Younger Dryas sea level and meltwater pulse 1B recorded in Barbados reef crest coral Acropora palmata. *Paleoceanography* **31**, 330–344 (2016). URL http://agupubs.onlinelibrary.wiley.com/doi/abs/10.1002/2015PA002847. _eprint: https://onlinelibrary.wiley.com/doi/pdf/10.1002/2015PA002847.

[54] Alley, R. B. & Ágústsdóttir, A. M. The 8k event: cause and consequences of a major Holocene abrupt climate change. *Quaternary Science Reviews* **24**, 1123–1149 (2005). URL https://www.sciencedirect.com/science/article/pii/S0277379105000314.

[55] Goehring, B. M., Balco, G., Todd, C., Moening-Swanson, I. & Nichols, K. Late-glacial grounding line retreat in the northern Ross Sea, Antarctica. *Geology* **47**, 291–294 (2019). URL https://doi.org/10.1130/G45413.1.

[56] Spector, P. *et al.* Rapid early-Holocene deglaciation in the Ross Sea, Antarctica. *Geophysical Research Letters* **44**, 7817–7825 (2017). URL https://onlinelibrary.wiley.com/doi/abs/10.1002/2017GL074216. _eprint: https://onlinelibrary.wiley.com/doi/pdf/10.1002/2017GL074216.

[57] Rand, C., Jones, R. S., Mackintosh, A. N., Goehring, B. & Lilly, K. A thicker-than-present East Antarctic Ice Sheet plateau during the Last Glacial Maximum. *The Cryosphere* **19**, 3681–3691 (2025). URL https://tc.copernicus.org/articles/19/3681/2025/.

[58] Golledge, N. R. *et al.* Antarctic contribution to meltwater pulse 1A from reduced Southern Ocean overturning. *Nature Communications* **5**, 5107 (2014). URL https://www.nature.com/articles/ncomms6107.

[59] Li, Q., Xiao, W., Wang, R. & Chen, Z. Diatom based reconstruction of climate evolution through the Last Glacial Maximum to Holocene in the Cosmonaut Sea, East Antarctica. *Deep Sea Research Part II: Topical Studies in Oceanography* **194**, 104960 (2021). URL https://www.sciencedirect.com/science/article/pii/S0967064521000369.

[60] Li, T. *et al.* Enhanced subglacial discharge from Antarctica during meltwater pulse 1A. *Nature Communications* **14**, 7327 (2023). URL https://www.nature.com/articles/s41467-023-42974-0.

[61] Pedro, J. B. *et al.* The spatial extent and dynamics of the Antarctic Cold Reversal. *Nature Geoscience* **9**, 51–55 (2016). URL https://www.nature.com/articles/ngeo2580.

[62] Manabe, S. & Stouffer, R. J. Coupled ocean-atmosphere model response to freshwater input: Comparison to Younger Dryas Event. *Paleoceanography* **12**, 321–336 (1997). URL https://onlinelibrary.wiley.com/doi/abs/10.1029/96PA03932. _eprint: https://agupubs.onlinelibrary.wiley.com/doi/pdf/10.1029/96PA03932.

[63] Cheng, H. *et al.* Timing and structure of the Younger Dryas event and its underlying climate dynamics. *Proceedings of the National Academy of Sciences* **117**, 23408–23417 (2020). URL https://www.pnas.org/doi/abs/10.1073/pnas.2007869117.

[64] Fudge, T. J. *et al.* Variable relationship between accumulation and temperature in West Antarctica for the past 31,000 years. *Geophysical Research Letters* **43**, 3795–3803 (2016). URL https://onlinelibrary.wiley.com/doi/abs/10.1002/2016GL068356. _eprint: https://agupubs.onlinelibrary.wiley.com/doi/pdf/10.1002/2016GL068356.

[65] Weber, M. E. *et al.* Millennial-scale variability in Antarctic ice-sheet discharge during the last deglaciation. *Nature* **510**, 134–138 (2014). URL https://www.nature.com/articles/nature13397.

[66] Velay-Vitow, J., Peltier, W. R., Stuhne, G. R. & Li, T. The hemispheric origins of meltwater pulse 1B. *Geophysical Journal International* **239**, 1021–1037 (2024). URL https://doi.org/10.1093/gji/ggae311.

[67] Buizert, C. *et al.* Antarctic surface temperature and elevation during the Last Glacial Maximum. *Science* **372**, 1097–1101 (2021). URL https://www.science.org/doi/10.1126/science.abd2897.

[68] Lambeck, K., Rouby, H., Purcell, A., Sun, Y. & Sambridge, M. Sea level and global ice volumes from the Last Glacial Maximum to the Holocene. *Proceedings of the National Academy of Sciences* **111**, 15296–15303 (2014). URL http://www.pnas.org/content/111/43/15296.

[69] Golledge, N. R. *et al.* Retreat of the Antarctic Ice Sheet During the Last Interglaciation and Implications for Future Change. *Geophysical Research Letters* **48**, e2021GL094513 (2021). URL https://onlinelibrary.wiley.com/doi/abs/10.1029/2021GL094513. _eprint: https://onlinelibrary.wiley.com/doi/pdf/10.1029/2021GL094513.

[70] Gregoire, L. J., Payne, A. J. & Valdes, P. J. Deglacial rapid sea level rises caused by ice-sheet saddle collapses. *Nature* **487**, 219–222 (2012). URL http://www.nature.com/articles/nature11257. Number: 7406.

[71] Matero, I. S. O., Gregoire, L. J., Ivanovic, R. F., Tindall, J. C. & Haywood, A. M. The 8.2 ka cooling event caused by Laurentide ice saddle collapse. *Earth and Planetary Science Letters* **473**, 205–214 (2017). URL https://www.sciencedirect.com/science/article/pii/S0012821X17303205.

[72] Renssen, H., Goosse, H., Crosta, X. & Roche, D. M. Early Holocene Laurentide Ice Sheet deglaciation causes cooling in the high-latitude Southern Hemisphere through oceanic teleconnection. *Paleoceanography* **25** (2010). URL https://onlinelibrary.wiley.com/doi/abs/10.1029/2009PA001854. _eprint: https://onlinelibrary.wiley.com/doi/pdf/10.1029/2009PA001854.

[73] Wiersma, A. P., Roche, D. M. & Renssen, H. Fingerprinting the 8.2 ka event climate response in a coupled climate model. *Journal of Quaternary Science* **26**, 118–127 (2011). URL https://onlinelibrary.wiley.com/doi/abs/10.1002/jqs.1439. _eprint: https://onlinelibrary.wiley.com/doi/pdf/10.1002/jqs.1439.

[74] Pedro, J. B. *et al.* Beyond the bipolar seesaw: Toward a process understanding of interhemispheric coupling. *Quaternary Science Reviews* **192**, 27–46 (2018). URL https://www.sciencedirect.com/science/article/pii/S0277379117310351.

[75] Pivel, M. A. G., Santarosa, A. C. A., Toledo, F. A. L. & Costa, K. B. The Holocene onset in the southwestern South Atlantic. *Palaeogeography, Palaeoclimatology, Palaeoecology* **374**, 164–172 (2013). URL https://www.sciencedirect.com/science/article/pii/S0031018213000357.

[76] Morrill, C. *et al.* Proxy benchmarks for intercomparison of 8.2 ka simulations. *Climate of the Past* **9**, 423–432 (2013). URL https://cp.copernicus.org/articles/9/423/2013/.

[77] Cheng, H. *et al.* Timing and structure of the 8.2 kyr B.P. event inferred from 18O records of stalagmites from China, Oman, and Brazil. *Geology* **37**, 1007–1010 (2009). URL http://pubs.geoscienceworld.org/geology/article/37/11/1007/29820/Timing-and-structure-of-the-82-kyr-BP-event.

[78] Rignot, E., Jacobs, S., Mouginot, J. & Scheuchl, B. Ice-Shelf Melting Around Antarctica. *Science (New York, N.Y.)* **341** (2013).

[79] Mawbey, E. M. *et al.* Ocean heat forced West Antarctic Ice Sheet retreat after the Last Glacial Maximum. *Nature Communications* (2026). URL https://www.nature.com/articles/s41467-026-68949-5.

[80] Behrens, B. C. *et al.* Beryllium isotope variations recorded in the Adélie Basin, East Antarctica reflect Holocene changes in ice dynamics, productivity, and scavenging efficiency. *Quaternary Science Advances* **7**, 100054 (2022). URL https://www.sciencedirect.com/science/article/pii/S2666033422000077.

[81] Denis, D. *et al.* Sea ice and wind variability during the Holocene in East Antarctica: insight on middle–high latitude coupling. *Quaternary Science Reviews* **29**, 3709–3719 (2010). URL https://www.sciencedirect.com/science/article/pii/S0277379110002957.

[82] Kim, M. *et al.* Holocene Palaeoenvironmental and Palaeoproductivity Changes in the Western Amundsen Sea Embayment of Antarctica. *Journal of Geophysical Research: Oceans* **128**, e2023JC019797 (2023). URL https://onlinelibrary.wiley.com/doi/abs/10.1029/2023JC019797. _eprint: https://onlinelibrary.wiley.com/doi/pdf/10.1029/2023JC019797.

[83] Kendall, R. A., Mitrovica, J. X., Milne, G. A., Törnqvist, T. E. & Li, Y. The sea-level fingerprint of the 8.2 ka climate event. *Geology* **36**, 423–426 (2008). URL https://pubs.geoscienceworld.org/gsa/geology/article-abstract/36/5/423/29785/the-sea-level-fingerprint-of-the-8-2-ka-climate.

[84] Dalton, A. S. *et al.* Deglaciation of the north American ice sheet complex in calendar years based on a comprehensive database of chronological data: NADI-1. *Quaternary Science Reviews* **321**, 108345 (2023). URL https://www.sciencedirect.com/science/article/pii/S0277379123003931.

[85] Briner, J. P. *et al.* Rate of mass loss from the Greenland Ice Sheet will exceed Holocene values this century. *Nature* **586**, 70–74 (2020). URL http://www.nature.com/articles/s41586-020-2742-6. Number: 7827.

[86] Ishiwa, T. *et al.* Re-evaluating Holocene ice-sheet thinning in the Indian Ocean sector of East Antarctica based on sea-level data and glacial isostatic adjustment modelling. *Quaternary Science Reviews* **375**, 109786 (2026). URL https://www.sciencedirect.com/science/article/pii/S0277379125006067.

[87] Jones, R. S., Gudmundsson, G. H., Mackintosh, A. N., McCormack, F. S. & Whitmore, R. J. Ocean-Driven and Topography-Controlled Nonlinear Glacier Retreat During the Holocene: Southwestern Ross Sea, Antarctica. *Geophysical Research Letters* **48**, e2020GL091454 (2021). URL https://onlinelibrary.wiley.com/doi/abs/10.1029/2020GL091454. _eprint: https://onlinelibrary.wiley.com/doi/pdf/10.1029/2020GL091454.

[88] Ashley, K. E. *et al.* Mid-Holocene Antarctic sea-ice increase driven by marine ice sheet retreat. *Climate of the Past* **17**, 1–19 (2021). URL https://cp.copernicus.org/articles/17/1/2021/.

[89] Lowry, D. P. *et al.* Ocean cavity regime shift reversed West Antarctic grounding line retreat in the late Holocene. *Nature Communications* **15**, 3176 (2024). URL https://www.nature.com/articles/s41467-024-47369-3.

[90] Venturelli, R. A. *et al.* Constraints on the Timing and Extent of Deglacial Grounding Line Retreat in West Antarctica. *AGU Advances* **4**, e2022AV000846

(2023). URL https://onlinelibrary.wiley.com/doi/abs/10.1029/2022AV000846. _eprint: https://onlinelibrary.wiley.com/doi/pdf/10.1029/2022AV000846.

[91] Venturelli, R. A. *et al.* Mid-Holocene Grounding Line Retreat and Readvance at Whillans Ice Stream, West Antarctica. *Geophysical Research Letters* **47**, e2020GL088476 (2020). URL https://onlinelibrary.wiley.com/doi/abs/10.1029/2020GL088476. _eprint: https://onlinelibrary.wiley.com/doi/pdf/10.1029/2020GL088476.

[92] Kingslake, J. Extensive Holocene West Antarctic Ice Sheet retreat and rebound driven re-advance. *Nature* (2018).

[93] Small, D. *et al.* A thinner-than-present West Antarctic Ice Sheet in the southern Weddell Sea Embayment during the Holocene. *The Cryosphere* **20**, 2035–2052 (2026). URL https://tc.copernicus.org/articles/20/2035/2026/.

[94] Nichols, K. A. *et al.* Direct Geologic Constraints on the Timing of Late Holocene Ice Thickening in the Amundsen Sea Embayment, Antarctica. *Geophysical Research Letters* **51**, e2024GL110350 (2024). URL https://onlinelibrary.wiley.com/doi/abs/10.1029/2024GL110350. _eprint: https://onlinelibrary.wiley.com/doi/pdf/10.1029/2024GL110350.

[95] Johnson, J. S. *et al.* Deglaciation of Pope Glacier implies widespread early Holocene ice sheet thinning in the Amundsen Sea sector of Antarctica. *Earth and Planetary Science Letters* **548**, 116501 (2020). URL https://www.sciencedirect.com/science/article/pii/S0012821X20304453.

[96] Rignot, E. *et al.* Four decades of Antarctic Ice Sheet mass balance from 1979–2017. *Proceedings of the National Academy of Sciences* **116**, 1095–1103 (2019). URL https://www.pnas.org/doi/abs/10.1073/pnas.1812883116.

[97] Pritchard, H. D. *et al.* Antarctic ice-sheet loss driven by basal melting of ice shelves. *Nature* **484**, 502–505 (2012).

[98] Lenaerts, J. T. M., Medley, B., van den Broeke, M. R. & Wouters, B. Observing and Modeling Ice Sheet Surface Mass Balance. *Reviews of Geophysics* **57**, 376–420 (2019). URL https://onlinelibrary.wiley.com/doi/abs/10.1029/2018RG000622. _eprint: https://agupubs.onlinelibrary.wiley.com/doi/pdf/10.1029/2018RG000622.

[99] Alley, R. B., Anandakrishnan, S., Dupont, T. K. & Parizek, B. R. Ice streams—fast, and faster? *Comptes Rendus Physique* **5**, 723–734 (2004). URL https://www.sciencedirect.com/science/article/pii/S1631070504001495.

[100] Weertman, J. Stability of the Junction of an Ice Sheet and an Ice Shelf. *Journal of Glaciology* **13**, 3–11 (1974). URL https://www.cambridge.org/core/product/identifier/S0022143000023327/type/journal_article.

[101] Pollard, D., DeConto, R. M. & Alley, R. B. Potential Antarctic Ice Sheet retreat driven by hydrofracturing and ice cliff failure. *Earth and Planetary Science Letters* **412**, 112–121 (2015). URL https://www.sciencedirect.com/science/article/pii/S0012821X14007961.

[102] Wingham, D. J., Wallis, D. W. & Shepherd, A. Spatial and temporal evolution of Pine Island Glacier thinning, 1995–2006. *Geophysical Research Letters* **36** (2009). URL https://onlinelibrary.wiley.com/doi/abs/10.1029/2009GL039126. _eprint: https://agupubs.onlinelibrary.wiley.com/doi/pdf/10.1029/2009GL039126.

[103] Golledge, N. R. *et al.* The multi-millennial Antarctic commitment to future sea-level rise. *Nature* **526**, 421–425 (2015). URL https://www.nature.com/articles/nature15706. Number: 7573.

[104] Lucas, E. M. *et al.* Emergence of Antarctic mineral resources in a warming world. *Nature Climate Change* 1–8 (2026). URL https://www.nature.com/articles/s41558-026-02569-1.

[105] Robel, A. A., Sim, S. J., Meyer, C., Siegfried, M. R. & Gustafson, C. D. Contemporary ice sheet thinning drives subglacial groundwater exfiltration with potential feedbacks on glacier flow. *Science Advances* **9**, eadh3693 (2023). URL https://www.science.org/doi/full/10.1126/sciadv.adh3693.

[106] Bosson, J. B. *et al.* Future emergence of new ecosystems caused by glacial retreat. *Nature* **620**, 562–569 (2023). URL https://www.nature.com/articles/s41586-023-06302-2.

[107] Hughes, K. A., Pertierra, L. R., Molina-Montenegro, M. A. & Convey, P. Biological invasions in terrestrial Antarctica: what is the current status and can we respond? *Biodiversity and Conservation* **24**, 1031–1055 (2015). URL https://doi.org/10.1007/s10531-015-0896-6.

[108] Tejedo, P. *et al.* What are the real environmental impacts of Antarctic tourism? Unveiling their importance through a comprehensive meta-analysis. *Journal of Environmental Management* **308**, 114634 (2022). URL https://www.sciencedirect.com/science/article/pii/S0301479722002079.

[109] Liggett, D., Cajiao, D., Lamers, M., Leung, Y.-F. & Stewart, E. J. The future of sustainable polar ship-based tourism. *Cambridge Prisms: Coastal Futures* **1**, e21 (2023). URL https://www.cambridge.org/core/journals/cambridge-prisms-coastal-futures/article/future-of-sustainable-polar-shipbased-tourism/121E454F668BCD14B615D834AAB62031.

[110] Brooks, S. T. *et al.* Systematic conservation planning for Antarctic research stations. *Journal of Environmental Management* **351**, 119711 (2024). URL https://www.sciencedirect.com/science/article/pii/S0301479723024994.

[111] McCarthy, A. H., Peck, L. S. & Aldridge, D. C. Ship traffic connects Antarctica's fragile coasts to worldwide ecosystems. *Proceedings of the National Academy of Sciences* **119**, e2110303118 (2022). URL https://www.pnas.org/doi/10.1073/pnas.2110303118.

[112] Stoeckl, N. *et al.* Governance challenges to protect globally important ecosystem services of the Antarctic and Southern Ocean. *ICES Journal of Marine Science* **82**, fsae163 (2025). URL https://doi.org/10.1093/icesjms/fsae163.

[113] Schaefer, J. M. *et al.* Cosmogenic nuclide techniques. *Nature Reviews Methods Primers* **2**, 1–22 (2022). URL https://www.nature.com/articles/s43586-022-00096-9.

[114] Lal, D. The present scope of the field of terrestrial cosmogenic nuclides. *Current Science* **61**, 744–751 (1991). URL https://www.jstor.org/stable/24095301.

[115] Stone, J. O. Air pressure and cosmogenic isotope production. *Journal of Geophysical Research: Solid Earth* **105**, 23753–23759 (2000). URL https://onlinelibrary.wiley.com/doi/abs/10.1029/2000JB900181. _eprint: https://onlinelibrary.wiley.com/doi/pdf/10.1029/2000JB900181.

[116] Desilets, D., Zreda, M. & Prabu, T. Extended scaling factors for in situ cosmogenic nuclides: New measurements at low latitude. *Earth and Planetary Science Letters* **246**, 265–276 (2006). URL https://www.sciencedirect.com/science/article/pii/S0012821X06002871.

[117] Dunai, T. J. Influence of secular variation of the geomagnetic field on production rates of in situ produced cosmogenic nuclides. *Earth and Planetary Science Letters* **193**, 197–212 (2001). URL https://www.sciencedirect.com/science/article/pii/S0012821X01005039.

[118] Lifton, N. A. *et al.* Addressing solar modulation and long-term uncertainties in scaling secondary cosmic rays for in situ cosmogenic nuclide applications. *Earth and Planetary Science Letters* **239**, 140–161 (2005). URL https://www.sciencedirect.com/science/article/pii/S0012821X05004437.

[119] Balco, G., Stone, J. O., Lifton, N. A. & Dunai, T. J. A complete and easily accessible means of calculating surface exposure ages or erosion rates from 10Be and 26Al measurements. *Quaternary Geochronology* **3**, 174–195 (2008). URL https://www.sciencedirect.com/science/article/pii/S1871101407000647.

[120] Nichols, K. A. *et al.* New Last Glacial Maximum ice thickness constraints for the Weddell Sea Embayment, Antarctica. *The Cryosphere* **13**, 2935–2951 (2019). URL https://tc.copernicus.org/articles/13/2935/2019/.

[121] Nichols, K. A. A decade of in situ cosmogenic 14C in Antarctica. *Annals of Glaciology* **63**, 67–72 (2022). URL https://www.cambridge.org/core/journals/annals-of-glaciology/article/decade-of-in-situ-cosmogenic-14c-in-antarctica/8CBB7484A4838C6572B666455415A4AB.

[122] Balco, G. Contributions and unrealized potential contributions of cosmogenic-nuclide exposure dating to glacier chronology, 1990–2010. *Quaternary Science Reviews* **30**, 3–27 (2011). URL https://www.sciencedirect.com/science/article/pii/S0277379110003999.

[123] Dyke, A. S. & Peltier, W. R. Forms, response times and variability of relative sea-level curves, glaciated North America. *Geomorphology* **32**, 315–333 (2000). URL http://www.sciencedirect.com/science/article/pii/S0169555X99001026.

[124] Jones, R. S., Small, D., Cahill, N., Bentley, M. J. & Whitehouse, P. L. iceTEA: Tools for plotting and analysing cosmogenic-nuclide surface-exposure data from former ice margins. *Quaternary Geochronology* **51**, 72–86 (2019). URL https://www.sciencedirect.com/science/article/pii/S1871101418301110.

[125] Ester, M., Kriegel, H.-P. & Xu, X. A Density-Based Algorithm for Discovering Clusters in Large Spatial Databases with Noise .

[126] Wingham, D. J., Wallis, D. W. & Shepherd, A. Spatial and temporal evolution of Pine Island Glacier thinning, 1995–2006. *Geophysical Research Letters* **36** (2009). URL https://onlinelibrary.wiley.com/doi/abs/10.1029/2009GL039126. _eprint: https://agupubs.onlinelibrary.wiley.com/doi/pdf/10.1029/2009GL039126.

[127] Boggs, P. T., Byrd, R. H. & Schnabel, R. B. A Stable and Efficient Algorithm for Nonlinear Orthogonal Distance Regression. *SIAM Journal on Scientific and Statistical Computing* **8**, 1052–1078 (1987). URL https://epubs.siam.org/doi/abs/10.1137/0908085.

Supplementary Files

This is a list of supplementary files associated with this preprint. Click to download.

- AISthinningMSsupplement.pdf